Risk-Averse Coordinated Operation of a Multi-Energy Microgrid Considering Voltage/Var Control and Thermal Flow: An Adaptive Stochastic Approach

Zhengmao Li, *Member, IEEE*, Lei Wu, *Senior Member, IEEE*, and Yan Xu, *Senior Member, IEEE*

***Abstract*—With an increasing penetration level of intermittent renewable energy sources and heterogeneous energy demands, the secure and economic operation of multi-energy microgrids (MEMGs) becomes more and more critical. Under this circumstance, this paper proposes an adaptive (two-layer) stochastic approach to obtain optimal MEMG operation decisions by taking advantage of distinct energy properties. First, rather than merely focusing on the active power economic dispatch, voltage/var control (VVC) scheme is involved to co-optimize the active and reactive power flow while guaranteeing voltage security; Second, a battery degradation model and a comprehensive thermal network model with thermal energy flow and transmission delay are presented to derive practical and efficient operations; Third, a conditional value-at-risk (CVaR)-based risk evaluation method is included to avoid over-optimistic solutions. The original nonlinear operation problem is reformulated as a mixed-integer linear programming (MILP) model to achieve high solution quality with acceptable computation performance. Finally, case studies are conducted to indicate that our proposed approach can effectively coordinate the dispatch of active/reactive power as well as thermal flow, thus ensuring system security with minimal operating costs and risks.**

***Index Terms*—Multi-energy microgrid, battery degradation, risk-averse adaptive stochastic, thermal network, voltage/var control.**

NOMENCLATURE

Abbreviations

BS	Battery storage
CB	Capacitor bank
CCHP	Combined cooling, heat, and power
CVaR	Conditional value-at-risk
DOD	Depth of discharge
MEMG	Multi-energy microgrid
MILP	Mixed-integer linear programming
OLTC	On-load tap change
PIA	Polygonal inner approximation
PtC	Power-to-thermal conversion
PV	Photovoltaic cell
RES	Renewable energy sources
RO	Robust optimization
SOC	Second-order cone
SP	Stochastic programming
TS	Thermal storage
VVC	Voltage/var control
WT	Wind turbine.

Sets and Indices

$Br(i,j)$	Branch/pipeline between nodes/buses i and j
n/i	Index of thermal nodes/power buses
N_I/N_B	The total number of power buses/branches
N_{SN}	Set of thermal source nodes
N_T	The total number of all dispatch periods
p/b	Index of thermal pipelines/power branches
$pair(p,n)$	Indicating pipeline p is connected with node n
$\mathbf{P}^{\mathbf{n}}_{\mathbf{s/r},(+)}$	Set of pipelines starting at node n in supply/return network at time t
$\mathbf{P}^{\mathbf{n}}_{\mathbf{s/r},(-)}$	Set of pipelines ending at node n in supply/return network at time t.

Parameters

C^i_{BS}	The capital cost of the *ith* BS
C_W	Water heat capacity
$DOD^{i,max}$	Maximal DOD of the *ith* BS
$E^{i,min}_{B/TS}/E^{i,max}_{B/TS}$	Min/max energy of the BS/ TS on bus i
$E^{i,R}_{BS}$	Rated capacity of the *ith* BS
$H^{i,min}_{TD}/H^{i,max}_{TD}$	Min/max releasing power of the TS on bus i
$H^{i,min}_{TC}/H^{i,max}_{TC}$	Min/max absorbing power of the TS on bus i
$H^{p,t}_{TL}$	Thermal demand at time t
$J^{p,t}_{s/r}$	The thermal loss coefficient of supply/return pipeline p at time t
$L^{i,R}_{BS}$	BS lifetime in terms of the number of life cycles
$N^{min}_{Tap}/N^{max}_{Tap}$	Min/max tap change ratio
$P^{i,min}_{BD}/P^{i,max}_{BD}$	Min/max discharging power of the BS on bus i

Manuscript received October 7, 2020; revised February 18, 2021 and April 8, 2021; accepted May 11, 2021. Date of publication May 14, 2021; date of current version August 23, 2021. This work was supported in part by the U.S. National Science Foundation under Grant CNS-1915756. Paper no. TSG-01494-2020. *(Corresponding author: Lei Wu.)*

Zhengmao Li and Lei Wu are with the ECE Department, Stevens Institute of Technology, Hoboken, NJ 07030 USA (e-mail: zli161@stevens.edu; lei.wu@stevens.edu).

Yan Xu is with the School of Electrical and Electronic Engineering, Nanyang Technological University, Singapore (e-mail: eeyanxu@gmail.com).

Color versions of one or more figures in this article are available at https://doi.org/10.1109/TSG.2021.3080312.

Digital Object Identifier 10.1109/TSG.2021.3080312

$P_{AC}^{b,min}/P_{AC}^{b,max}$ Min/max active power flow of branch b
$P_{PtC}^{i,max}$ Maximum power input of the PtC unit on bus i
$P_{BC}^{i,min}/P_{BC}^{i,max}$ Min/max charging power of the BS on bus i
$P_{MT}^{i,min}/P_{MT}^{i,max}$ Min/max power output of the CCHP plant on bus i
$P_{EL}^{t,i}/Q_{RL}^{t,i}$ Active/reactive power load on bus i at time t
$Q_{RE}^{b,min}/Q_{RE}^{b,max}$ Min/max reactive power flow of branch b
$Q_{WT}^{i,max}/Q_{PV}^{i,max}$ Maximum reactive power of the WT/PV on bus i
$Q_{CB}^{i,min}/Q_{CB}^{i,max}$ Min/max reactive power of the CB on bus i
$Q_{MT}^{i,min}/Q_{MT}^{i,max}$ Min/max reactive power of the CCHP plant on bus i
r^b/x^b Resistance/reactance of branch b
$R_{MT}^{i,max}$ Maximum ramp rate of the CCHP plant on bus i
S_{PF}^b Apparent power of branch b
S_{MT}^i Apparent power of the CCHP plant on bus i
S_{WT}^i/S_{PV}^i Apparent power of the WT/PV on bus i
$T_{s/r,(+)/(-)}^{max}$ Max temperature at the start/end of a supply/return pipeline
$T_{s/r,(+)/(-)}^{min}$ Min temperature at the start/end of a supply/return pipeline
T_q^t Ambient temperature at time t
V_{CB}^i/V_{Tap} Unit adjustment level of the CB on bus i / OLTC
$V_{BUS}^{i,min}/V_{BUS}^{i,max}$ Min/max nodal voltage magnitude on bus i
V_s Voltage of the substation
Δt Unit dispatch interval
η_{BC}/η_{BD} BS charging/discharging efficiency
η_{TC}/η_{TD} TS absorbing/releasing efficiency
λ_p Thermal transfer coefficient
ξ_{DC}^i BS degradation cost per charging/discharging event
ξ_{PtC}^M/ξ_{TS}^M Unit maintenance cost of a PtC unit/TS
$\xi_{WT}^M/\xi_{PV}^M/\xi_{BS}^M$ Unit maintenance cost of a WT/PV/BS
ξ_{NG}/ξ_{PL} Unit gas price/power loss cost
$\xi_{MT}^{U,i}/\xi_{MT}^M$ Unit CCHP start-up cost on bus i /maintenance cost
ρ_c/α_c Weight for risk/system confidential level
τ_B/τ_s Power purchasing/selling price
τ_{BS}/τ_{TS} Decay rate of a BS/TS.

Variables

C_F Total MEMG operation cost
C_{EX}^t/C_{ST}^t Power exchanging/startup cost at time t
$C_{FU}^t/C_{OM}^t/C_{PL}^t$ Fuel/maintenance/power loss cost at time t
$CVaR_\alpha(C_F)$ System CVaR level
$H_{s/r,(+)/(-)}^{p,t}$ Thermal energy at start/end of supply/return pipeline p at time t
$H_{PtC}^{t,i}/H_{MT}^{t,i}$ Thermal output of the PtC unit/CCHP plant on bus i at time t
$H_{TC}^{t,i}/H_{TD}^{t,i}$ TS absorbing/releasing power on bus i at time t
$m_{s/r}^{p,t}$ Mass flow rate of the supply/return pipeline p at time t
N_{CB}^t/N_{Tap}^t Position level of a CB/OLTC at time t
P_{BUY}^t/P_{SELL}^t Purchasing/selling power at time t
$P_{AC}^{t,0,b}/Q_{RE}^{t,0,b}$ Active/reactive power through the lateral branch of branch b at time t
$P_{AC}^{t,b}/Q_{RE}^{t,b}$ Active/reactive power flow of branch b at time t
$P_{BC}^{t,i}/P_{BD}^{t,i}$ BS charging/discharging power on bus i at time t
$P_{MT}^{t,i}/Q_{MT}^{t,i}$ Active/reactive power output of the CCHP plant on bus i at time t
$P_{PtC}^{t,i}$ Power input of the PtC unit on bus i at time t
$P_{WT}^{t,i}/P_{PV}^{t,i}$ Active power output of the WT/PV on bus i at time t
$Q_{CB}^{t,i}$ Active power output from the CB on bus i at time t
$Q_{WT}^{t,i}/Q_{PV}^{t,i}$ Reactive power from the WT/PV on bus i at time t
$T_{s/r}^{n,t}$ Temperature of node n of supply/return network at time t
$T_{s/r,(-)}^{p,t}$ Actual temperature at the end of the pipeline p at time t
$T_{s/r,(-)*}^{p,t}$ Equivalent temperature at the end of the pipeline p at time t
$T_{s/r,(+)}^{p,t}/T_{s/r,(-)}^{p,t}$ Temperature at start/end of the pipeline p at time t
$U_{MT}^{t,i}$ On/off status of the CCHP plant on bus i at time t
$V_{BUS}^{t,i}$ Bus voltage on bus i at time t
η_{VaR} Value at risk.

I. Introduction

CENTERED in the radial power distribution network, the current MEMGs, though are usually in small scales, can integrate heterogeneous energy carriers such as the power and thermal (e.g., heat and/or cooling) energy to enhance the holistic energy utilization efficiency [1]. Meanwhile, the growing penetration of fluctuating RES would introduce high uncertainties that greatly complicate the MEMG operations. In this light, new approaches to leverage the distinct energy properties and tackle the diverse uncertainties have attracted significant research both in academia and industry to achieve secure and efficient MEMG operations.

In the literature, to mitigate the adverse effects from various uncertainties, RO and SP methods are typically utilized [2]. In [3], a RES-based MEMG is studied to reduce the total system operation cost and immune against all uncertainties via the RO method. The study in [4] proposes an optimal robust dispatch model for a community MEMG, which aims to reduce the total operation cost under various uncertainties from electric vehicles and electricity prices. Reference [5] presents an optimal robust operation model to manage MEMGs with electrical and heat energy demands. It aims to reduce the total cost of MEMGs while mitigating the adverse effects from uncertainties under their worst-case realizations. The study in [3]–[5] focuses on the uncertainty immunization for day-ahead operations, but both neglect the actual intra-day operations when uncertainties are gradually realized throughout the day. In this regard, an adaptive or two-layer framework

shall be applied to coordinate both the day-ahead and intra-day operation by leveraging the simulated uncertainties and their actual realizations. Reference [6] presents a two-stage RO model to coordinate all units in an islanded MEMG for minimizing the operation cost and immunizing against diverse system uncertainties. Aiming at minimizing the multi-energy supplying cost, Reference [7] uses a multi-stage RO method to tackle various uncertainties of a MEMG in both grid-tied and islanded modes. The study in [8] discusses an improved adaptive RO-based bidding strategy for a MEMG to maximize its operation benefit or minimize its costs with characterized system uncertainties. Though the day-ahead and intra-day operations are coordinated in [6]–[8], RO decisions against worst cases could be overly conservative as the occurrence probability of the worst-case scenario would be extremely low in practice [2].

In comparison, the SP method, which calculates the expected system operation cost over a set of uncertainty scenarios and hence avoids too conservative decisions, can be utilized. In [9], to handle uncertainties from RESs, power transaction prices, and energy demands, the scheduling problem for a MEMG with multiple assets is evaluated via the SP approach. However, only the day-ahead operation is considered. The study in [10] adopts an SP method to obtain the optimal scheduling of a residential MEMG while considering RES uncertainties. Reference [11] proposes a multiple-timescale coordinated stochastic approach for a MEMG with CCHP plants and wind farms in a deregulated day-ahead heat market and a real-time balancing electricity market. In [12], the temporal coordination of multiple energy in a MEMG via the two-stage SP method is investigated. It minimizes system operation costs and alleviates the adverse effects of various uncertainty sources. However, SP solutions could be overly optimistic because the low-probability high-impact uncertainty scenarios are usually excluded via the scenario reduction methods for alleviating computational burden [11]. To this end, proper risk measurements shall be integrated into the SP method to limit the covariance of solutions among different scenarios and avoid over-optimistic decisions [13].

Moreover, all the research works above merely focus on the active power scheduling, however, the active and reactive power in MEMGs is in practice closely intertwined because of high resistance-to-reactance ratios of distribution lines [14]. In this sense, those separate research may not be effective enough for the coordinated power management in practice. The reactive power is mainly dispatched via the VVC, which is an important technique for stabilizing voltage, minimizing power losses, and improving operational efficiency [15], especially when the system is exposed to deeper penetration of RESs. The VVC scheme can be implemented in a decentralized form with the local information [16]. Although fast and simple, there is a lack of coordination for the entire system. Alternatively, centralized forms could coordinate the heterogeneous VVC devices based on the system-wide information to satisfy voltage requirements. The study in [17] presents an optimal multi-objective VVC method for distribution systems while considering the number of tap movements of transformers and active power curtailment of RESs. Reference [18] proposes a VVC method for the optimal dispatch of BS in a distribution system. It coordinates the different assets via a model predictive control-based SP approach. In [19], a three-step method of the global search, user preference, and local search is used to solve the VVC problem with uncertainties. In [20], optimal energy management for a multi-energy virtual power plant is studied to minimize the operation cost and alleviate the adverse effects from various uncertainty sources via the risk-constrained single-layer SP method. However, studies in [14]–[20] mainly focus on the reactive power coordination, while neglecting the multi-layer scheduling of reactive power devices such as OLTCs, CBs, and electronic converters. That is, no VVC is considered. Thus, they cannot derive effective operation strategies for MEMGs with a highly intertwined relationship between active and reactive power.

In addition, though centered in the power grid, the thermal energy management in the MEMGs can be equally important. As compared to electric energy, thermal energy presents the following distinct characters [12].

(i) The thermal transmission delay is nontrivial: Compared with the instantaneous electricity transmission, it takes time to deliver hot/cold water (as the main heat transmission media) from sources to loads through thermal pipelines.

(ii) The intrinsic thermal insulation abilities of the buildings and water pipelines can facilitate the supply-demand balance of the thermal energy [20].

Thus, the thermal network should be thoroughly modelled for more comprehensive and realistic system operations, by leveraging different energy properties for uncertainty immunization and cost reduction purposes. However, detailed thermal network models are usually neglected [3], [7]–[9], [11], [20] or simplified [21] in the related multi-energy research.

Moreover, given the nonlinear nature of operation models for MEMGs, intelligent algorithms [13], [17]–[18] and nonlinear solvers [11], [14], [19] are commonly used. Nonetheless, intelligent algorithms can be computationally expensive and highly dependent on the initial conditions with convergence concerns, while nonlinear solvers cannot always guarantee global optimality. In addition, the battery degradation model, which is a significant factor for the practical BS operation and protection, is not effectively involved in most of the related research.

Given the above insights, to fill in the research gap, this paper studies a risk-averse adaptive (two-layer) SP method for the coordinated operation of MEMGs. The main research contents and contributions of this paper can be listed as below.

(i) The comprehensive coordination model for the MEMG under heterogeneous uncertainties is proposed while considering the VVC scheme, and realistic thermal network constraints and battery degradation at the same time. Hence, the active/reactive power and thermal energy are co-scheduled on the system-wide scale for a more realistic, secure, and economic operation. To the best of our knowledge, no such comprehensive research work has been done for the emerging MEMGs in the literature.

(ii) A two-layer (adaptive) risk-averse SP approach for the optimal coordination of VVC assets, distributed generators, and storage devices is presented to addresses diverse

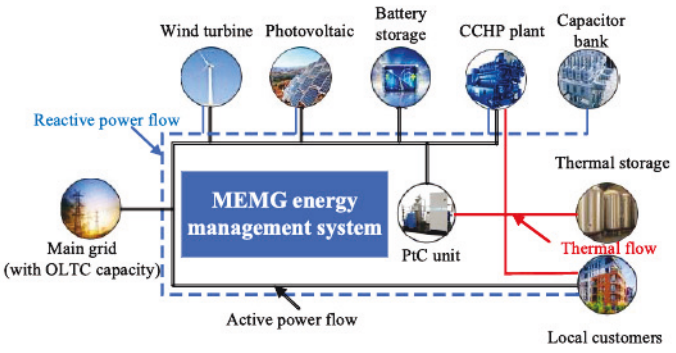

Fig. 1. The typical structure of a MEMG.

uncertainties and avoids over-optimistic or too-pessimistic decisions. The two-layer (adaptive) method can effectively address the interplay of MEMG operations in both the day-ahead and intra-day timeframes. Furthermore, though the risk-averse SP approach is used in areas such as the large power gird or virtual power plant operation [20], [22], frequency regulation market [23], and wireless communication network [24], its performance in coordinating the economic active power dispatch, VVC scheme, and practical thermal scheduling on a MEMG system-wide scale is not fully investigated yet in the literature.

(iii) For better computational performance, the original nonlinear and/or nonconvex formulations are convexified/ linearized via the appropriate methods to derive a MILP model. It can be effectively solved by industry-proven MILP solvers with favorable computation time and solution quality.

The rest of the paper is organized as follows. The MEMG model is discussed in Section II. Sections III and IV present the proposed risk-averse coordinated operation model and solution approach. Numerical case studies are conducted in Section V, and the conclusions are drawn in Section VI.

II. Multi-Energy Microgrid Modelling

A. Multi-Energy Microgrid Structure

The typical structure of a grid-tied MEMG is shown in Fig. 1. In the MEMG, thermal loads are supplied by CCHP plants, PtC units. As for the electrical demands, besides the powerful support from the main grid, active power loads are also supplied by the CCHP plants, WTs, and PVs [5]. The OLTCs, CBs, and electronic converters of all distributed generators are responsible for the reactive power support [11]. Heterogeneous energy storage assets including BS and TS could contribute to the load shifting and dispatch flexibility enhancement via the charging (absorbing)/discharging(releasing) processes [12].

B. Multi-Energy Conversion Modelling

An energy conversion block also called an energy hub [25], is utilized to describe multi-energy coordination. The general model of the energy conversion block is shown in (1). The gas energy input P_G is consumed by CCHP plants to produce power and thermal energy simultaneously, with the efficiencies

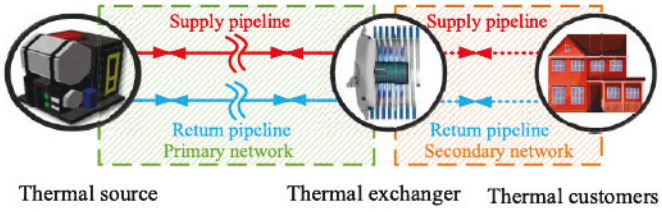

Fig. 2. A general structure of the thermal network.

η_{ME} and η_{MT}. The power P_E from the main grid, RES, and CCHP plants can also be converted into thermal energy via the PtC units with efficiency η_{PtC}.

$$\underbrace{\begin{bmatrix} P_{EL} \\ H_{TL} \end{bmatrix}}_{Outputs} = \underbrace{\begin{bmatrix} \eta_{ME} & 1 \\ \eta_{MT} & \eta_{PtC} \end{bmatrix}}_{EnergyConversionBlock} \cdot \underbrace{\begin{bmatrix} P_G \\ P_E \end{bmatrix}}_{Inputs} \tag{1}$$

C. Realistic Thermal Network Modelling

A typical thermal network structure can be shown in Fig. 2. It usually contains one source node and multiple immediate/load nodes connected via supply pipelines (*i.e.*, primary network) and return pipelines (i.e., secondary network). The thermal energy is delivered via water through supply pipelines, after entering the thermal exchanger in the secondary network, the thermal energy is transmitted to load nodes and water temperature dramatically changes. Finally, the water flows back through return pipelines to complete the thermal circulation [21]. Compared with the primary network, pipelines in the secondary network are short and thus not modelled in detail.

- *Nodal flow balance:* Thermal flow follows the *Kirchhoff* law, i.e., the amount of water entering in one node is equal to the corresponding outflows as in (2).

$$\sum_{p \in \mathbf{P}^{n}_{s/r,(-)}} m^{p,t}_{s/r} = \sum_{p \in \mathbf{P}^{n}_{s/r,(+)}} m^{p,t}_{s/r}, \quad p \in Br(n, n+1) \tag{2}$$

- *Nodal temperature mixing:* According to *the first law of thermodynamics*, the nodal temperature depends on the water mass and temperature of all connected pipelines [19] as in (3). Besides, the temperature of a given node is equal to that of the start node of the same pipeline as in (4).

$$\sum_{p \in \mathbf{P}^{n}_{s/r,(-)}} \left(T^{p,t}_{s/r,(-)} \cdot m^{p,t}_{s/r} \right) = T^{n,t}_{s/r} \cdot \left(\sum_{p \in \mathbf{P}^{n}_{s/r,(+)}} m^{p,t}_{s/r} \right) \tag{3}$$

$$T^{n,t}_{s/r} = T^{p,t}_{s/r,(+)}, pair(p, n) \tag{4}$$

- *Thermal energy calculation:* The exact thermal energy in each pipeline can be calculated via (5).

$$H^{p,t}_{s/r,(-)/(+)} = C_W \cdot m^{p,t}_{s/r} \cdot T^{p,t}_{s/r,(-)/(+)} \tag{5}$$

- *Thermal transmission delay:* Given the pipeline length and mass flow rate, the thermal transmission is dynamic, i.e., with transmission delays [19]. The vertical section in Fig. 3 of a supply pipeline can be used to explain this dynamic effect.

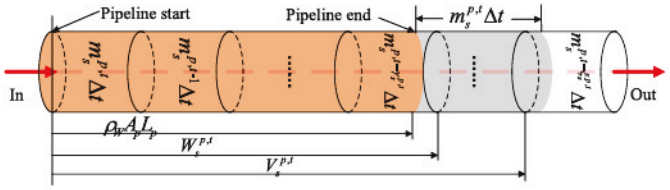

Fig. 3. The vertical section of a supply pipeline.

In Fig. 3, with the length L_p and area A_p for the cross-section of the *pth* pipeline, the water volume is $\rho_W A_p L_p$ (ρ_W is water density). The orange and gray volumes denote water flowing in and out. For example, $m_s^{p,t} \cdot \Delta t$ denotes the water mass flowing into the *pth* pipeline at time *t*. The block on the right end of the pipeline is water mass that has flowed out by the end of time *t*. That is, after time $\gamma_s^{p,t}$, water starts to flow out; while after $\xi_s^{p,t}$, the entire water mass completely flows out. Given the above flow rate and pipeline information, $\gamma_s^{p,t}$, and $\xi_s^{p,t}$ are calculated as in (6) and (8), where t_p is a decision variable.

$$\gamma_s^{p,t} = \min_{t_m \in N_T} t_m \tag{6}$$

$$s.t., \sum\nolimits_{t_p=t-t_m}^{t} m_s^{p,t_p} \cdot \Delta t \geq \rho_W \cdot A_p \cdot L_p \tag{7}$$

$$\xi_s^{p,t} = \min_{t_n \in N_T} t_n \tag{8}$$

$$s.t., \sum\nolimits_{t_p=t-t_n}^{t} \left(m_s^{p,t_p} \cdot \Delta t \right) \geq \rho_W \cdot A_p \cdot L_p + m_s^{p,t} \cdot \Delta t \tag{9}$$

Accordingly, $W_s^{p,t}$, and $V_s^{p,t}$ represent the total water mass flowing into the pipeline during periods $[t - \gamma_s^{p,t}, t]$ and $[t - \xi_s^{p,t}, t]$, which can be respectively calculated as in (8) and (9).

$$W_s^{p,t} = \sum\nolimits_{t_p=t-t_m}^{t} \left(m_s^{p,t_p} \cdot \Delta t \right) \tag{10}$$

$$V_s^{p,t} = \begin{cases} \sum_{t_p=t-t_n+1}^{t} \left(m_s^{p,t_p} \cdot \Delta t \right), & t_n \geq t_m + 1 \\ W_s^{p,t}, & t_n < t_m + 1 \end{cases} \tag{11}$$

To this end, the equivalent temperature at the terminal of a pipeline, *i.e.*, the outflow water temperature, can be estimated as the average temperature of water in the grey volume of Fig. 3:

$$T_{s/r,(-)*}^{p,t} = \left[\begin{array}{l} \left(m_{s/r}^{p,t} \cdot \Delta t + \rho_W \cdot A_p \cdot L_p - V_{s/r}^{p,t} \right) \cdot T_{s/r,(+)}^{p,t-\xi_{p,t}^{s/r}} \\ + \sum_{t_p=t-\xi_{p,t}^{s/r}+1}^{t-\gamma_{p,t}^{s/r}-1} \left(m_{s/r}^{p,t_p} \cdot \Delta t \cdot T_{s/r(+)}^{p,t_p-\xi_{p,t}^{s/r}} \right) \\ + \left(W_{s/r}^{p,t} - \rho_W \cdot A_p \cdot L_p \right) \cdot T_{s/r,(+)}^{p,t-\gamma_{p,t}^{s/r}} \end{array} \right] / \left(m_{s/r}^{p,t} \cdot \Delta t \right) \tag{12}$$

- *Thermal transmission losses:* To consider the actual energy losses due to thermal exchange with pipeline shells [neglected in (12)], the outflow temperature can be revised based on *Shukhov's Temperature Loss Law* as in (13).

$$T_{s/r,(-)}^{p,t} = T_a^t + J_{s/r}^{p,t} \cdot \left(T_{s/r,(-)*}^{p,t} - T_a^t \right)$$
$$J_{s/r}^{p,t} = \exp\left[-\frac{\lambda_p \cdot \Delta t}{A_p \cdot \rho_W \cdot C_W} \left(\gamma_{s/r}^{p,t} + 1/2 + \frac{V_{s/r}^{p,t} - W_{s/r}^{p,t}}{m_{s/r}^{p,t-\gamma_{p,t}^{s/r}} \cdot \Delta t} \right) \right] \tag{13}$$

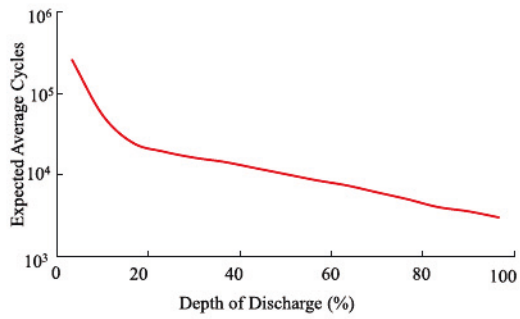

Fig. 4. Typical DOD vs. cycle life curve of battery storage.

- *Internal temperature range:* In a pipeline, the inflow and outflow water temperature are bounded as in (14).

$$T_{s/r,(-)/(+)}^{\min} \leq T_{s/r,(-)/(+)}^{p,t} \leq T_{s/r,(-)/(+)}^{\max} \tag{14}$$

- *Thermal energy balance:* The thermal energy generation and consumption shall be balanced all the time. The thermal demands are satisfied by dispatching thermal network generation sources, mass flow rates, and pipeline temperature [21], [26]. As thermal energy is carried by hot/cold water (the main heat transmission media) from sources to loads through thermal pipelines, the total thermal energy need is equal to the energy difference between the start of supply pipelines and the end of return pipelines, as described in (15) [19].

$$H_{TL}^{p,t} = C_W \cdot \left(m_s^{p,t} \cdot T_{s/r,(+)}^{p,t} - m_r^{p,t} \cdot T_{s/r,(-)}^{p,t} \right), p \in \mathbf{N_{SN}} \tag{15}$$

D. Battery Degradation Modelling

Degradation is one of the most important factors for the practical BS operation. In the literature, many BS degradation models have been conducted as the BS aging mechanism is a rather complex process [27]. References [28] and [29] model the nonlinear BS degradation cost with respect to its DOD and lifetime. In [30], the ambient temperature and DOD are used to calculate the BS degradation cost. References [31] and [32] utilize the BS cycle life and maximal DOD to formulate the degradation cost into equal payment for individual charging and discharging events.

To evaluate the overall BS performance, a key criterion is the life cycle, which is denoted as the number of charging/discharging cycles that the BS can perform before its capacity falls below 80% of its rated capacity [31]. The BS cycle life generally has a logarithmic relationship with the DOD, and the number of life cycles goes up exponentially as the DOD reduces [33]. A typical curve of BS life cycles $L_{BS}^{i,R}$ under different DODs is shown in Fig. 4.

Based on [31]–[33], the BS degradation cost per charging or discharging event can be denoted as (16):

$$\xi_{DC}^{i} = \frac{\text{Battery replacement cost}}{\text{Total energy throughput during lifecycle}} \tag{16}$$

Given the above definition, the mathematical formulation for the BS degradation cost per charging or discharging event is

presented in (17). The factor of 2 in the denominator accounts for the degradation cost both due to the charging and discharging events. Give specific parameters for BSs from the manufacturer, the unit degradation cost per charging or discharging event can be calculated via curve fitting methods. The details can be referred to [33].

$$\xi_{DC}^{i} = \frac{C_{BS}^{i} \cdot E_{BS}^{i,R}}{2 \cdot L_{BS}^{i}\left(DOD^{i,\max}\right) \cdot E_{BS}^{i,R}} \tag{17}$$

As for the TSs, it is usually in the form of thermal tanks whose degradation could be negligible. Thus, no degradation cost for TSs is involved in this study.

III. Risk-Averse Stochastic Coordinated Operation of Multi-Energy Microgrids

A. The Risk-Averse Stochastic Coordination Model of MEMG

The proposed risk-averse stochastic multi-energy coordination model of MEMGs is described in Eqs. (18)-(52). It minimizes the expected weighted sum of operation cost and risks (18) over the uncertainties, subject to prevailing operation constraints. The system operation cost (19) includes fuel cost (20), maintenance cost (21), the start-up cost of CCHP plants (22), power losses cost (23), power transaction cost with the main grid (24), and the BS degradation cost (25). The risk in terms of the CVaR is formulated as in Eq. (26). It constitutes a threshold to recognize (1-α_c)*100 percent of the worst scenarios of a stochastic environment [13].

Thermal flow constraints are described in Eq. (27). Eq. (28) is the thermal energy balance; Eq. (29) describes the relationship between power and thermal energy for CCHP plants and PtC units. The *Dist-Flow* model in Eqs. (30)-(40) is used to calculate the power flow. In the *Dist-Flow* model, power losses of branches are temporarily neglected for the sake of computational simplicity [14]. After the branch flows are determined, power losses can be re-calculated as in Eq. (23). The accuracy and effectiveness of *Dist-Flow* models have been extensively justified in the literature [33]. Eqs. (30) and (31) describe the active and reactive power balance condition; Eq. (32) calculates system nodal voltages; Eq. (33) restricts the power flow and voltage limits; Eq. (34) states the line capacity limits; Eq. (35) indicates that the reference bus voltage can be changed by OLTCs with respect to tap position limits; Eq. (37) describes reactive power provision abilities of CBs; Eqs.(38)-(40) are the capacity and reactive power limits of CCHP plants, WTs, and PVs; Eq. (41) presents the active power output/input limits of CCHP plants and PtC units. Eq. (42) is the ramping limits of CCHP plants. Eq. (43) describes the power exchange limits of MEMG with the main grid. Eqs.(45)-(48) are the operation limits of BSs, where Eq. (45) describes the safe ranges of charging and discharging power/energy; Eq. (46) represents exclusive charging and discharging; Eq. (47) denotes energy balance of BSs; Eq. (48) restricts the same initial and terminal energy for achieving the consistent dispatch flexibility in each daily operation cycle [8]. Similar to BSs, the operation constraints of TSs are formulated in Eqs. (49)-(52).

$$\min_{\mathbf{P,E,Q,H,U,V,T,m}} \mathbf{E}\left[\underbrace{C_F}_{\text{operation cost}}\right] + \rho_c \cdot \underbrace{CVaR_{\alpha}(\mathbf{E}[C_F])}_{\text{risk}} \tag{18}$$

$$C_F = \sum_{t \in N_T}\left(C_{FU}^{t} + C_{OM}^{t} + C_{ST}^{t} + C_{PL}^{t} + C_{EX}^{t} + C_{DC}^{t}\right) \cdot \Delta t \tag{19}$$

$$C_{FU}^{t} = \sum_{i \in N_I} \xi_{NG} \cdot P_{MT}^{t,i} / \eta_{ME} \tag{20}$$

$$C_{OM}^{t} = \sum_{i \in N_I}\left[\begin{array}{c} \xi_{MT}^{M} \cdot P_{MT}^{t,i} + \xi_{PtC}^{M} \cdot P_{PtC}^{t,i} + \xi_{WT}^{M} \cdot P_{WT}^{t,i} + \xi_{PV}^{M} \cdot P_{PV}^{t,i} \\ + \xi_{BS}^{M} \cdot \left(P_{BC}^{t,i} + P_{BD}^{t,i}\right) + \xi_{TS}^{M} \cdot \left(H_{TC}^{t,i} + H_{TD}^{t,i}\right) \end{array}\right] \tag{21}$$

$$C_{ST}^{t} = \sum_{i \in N_I} \max\left\{0, U_{MT}^{t,i} - U_{MT}^{t-1,i}\right\} \cdot \xi_{MT}^{U,i} \tag{22}$$

$$C_{PL}^{t} = \xi_{PL} \cdot \sum_{b \in N_B} r^{b} \cdot \left[\left(P_{AC}^{t,b}\right)^2 + \left(Q_{RE}^{t,b}\right)^2\right] / V_S^2,\ b \in Br(i, i{+}1) \tag{23}$$

$$C_{EX} = \sum_{t \in N_T}\left(\tau_B \cdot P_{BUY}^{t} - \tau_S \cdot P_{SELL}^{t}\right) \cdot \Delta t \tag{24}$$

$$C_{DC}^{t} = \sum_{i \in N_I} \xi_{DC}^{i} \cdot \left(P_{BC}^{t,i} + P_{BD}^{t,i}\right) \tag{25}$$

$$CVaR_{\alpha}(\mathbf{E}[C_F]) = \eta_{VaR} + \mathbf{E}[\max(C_F - \eta_{VaR}, 0)]/(1 - \alpha_c) \tag{26}$$

$$\text{Equations. (2)} - \text{(15)} \tag{27}$$

$$H_{TL}^{p,t} = H_{MT}^{t,i} + H_{PtC}^{t,i} - H_{TC}^{t,i} + H_{TD}^{t,i}, \quad pair(p, i) \tag{28}$$

$$\left[H_{MT}^{t,i}, H_{PtC}^{t,i}\right] = \left[P_{MT}^{t,i}, P_{PtC}^{t,i}\right] \cdot [\eta_{MT}, \eta_{PtC}] \tag{29}$$

$$P_{AC}^{t,b+1} = \left[\begin{array}{c} P_{AC}^{t,b} - P_{AC}^{t,0,b+1} - P_{EL}^{t,i} + P_{WT}^{t,i} + \\ P_{PV}^{t,i} + P_{BD}^{t,i} - P_{BC}^{t,i} + P_{MT}^{t,i} - P_{PtC}^{t,i} \end{array}\right] \tag{30}$$

$$Q_{RE}^{t,b+1} = Q_{RE}^{t,b} - Q_{RE}^{t,0,b+1} - Q_{RL}^{t,i} + Q_{CB}^{t,i} + Q_{WT}^{t,i} + Q_{PV}^{t,i} + Q_{MT}^{t,i} \tag{31}$$

$$V_{BUS}^{t,i+1} = V_{BUS}^{t,i} - \left(r^{b} \cdot P_{AC}^{t,b} + x^{b} \cdot Q_{RE}^{t,b}\right)/V_S \tag{32}$$

$$\left[P_{AC}^{t,b}, Q_{RE}^{t,b}, V_{BUS}^{t,i}\right] \begin{cases} \geq \left[P_{AC}^{b,\min}, Q_{RE}^{b,\min}, V_{BUS}^{i,\min}\right] \\ \leq \left[P_{AC}^{b,\max}, Q_{RE}^{b,\max}, V_{BUS}^{i,\max}\right] \end{cases} \tag{33}$$

$$\left(P_{AC}^{t,b}\right)^2 + \left(Q_{RE}^{t,b}\right)^2 \leq \left(S_{PF}^{b}\right)^2 \tag{34}$$

$$V_{BUS}^{t,0} = V_S + N_{Tap}^{t} \cdot V_{Tap} \tag{35}$$

$$N_{Tap}^{\min} \leq N_{Tap}^{t} \leq N_{Tap}^{\max} \tag{36}$$

$$Q_{CB}^{i,\min} \leq Q_{CB}^{t,i} = N_{CB}^{t} \cdot V_{CB}^{i} \leq Q_{CB}^{i,\max} \tag{37}$$

$$\left(P_{MT}^{t,i}\right)^2 + \left(Q_{MT}^{t,i}\right)^2 \leq \left(S_{MT}^{i}\right)^2 \tag{38}$$

$$\left[\left(P_{WT}^{t,i}\right)^2 + \left(Q_{WT}^{t,i}\right)^2, \left(P_{PV}^{t,i}\right)^2 + \left(Q_{PV}^{t,i}\right)^2\right] \leq \left[\left(S_{WT}^{i}\right)^2, \left(S_{PV}^{i}\right)^2\right] \tag{39}$$

$$\left[Q_{MT}^{i,\min}, 0, 0\right] \leq \left[Q_{MT}^{t,i}, Q_{WT}^{t,i}, Q_{PV}^{t,i}\right] \leq \left[Q_{MT}^{i,\max}, Q_{WT}^{i,\max}, Q_{PV}^{i,\max}\right] \tag{40}$$

$$\left[P_{MT}^{i,\min} U_{MT}^{t,i}, 0\right] \leq \left[P_{MT}^{t,i}, P_{PtC}^{t,i}\right] \leq \left[P_{MT}^{i,\max} U_{MT}^{t,i}, P_{PtC}^{i,\max}\right] \tag{41}$$

$$\pm\left(P_{MT}^{t,i} - P_{MT}^{t-1,i}\right) \leq R_{MT}^{i,\max} \cdot \Delta t \tag{42}$$

$$P_{BUY}^{t} - P_{SELL}^{t} = P_{AC}^{t,1} \tag{43}$$

$$P_{BUY}^{t} \cdot P_{SELL}^{t} = 0 \tag{44}$$

$$\left[P_{BC}^{t,i}, P_{BD}^{t,i}, E_{BS}^{t,i}\right] \begin{cases} \geq \left[P_{BC}^{i,\min}, P_{BD}^{i,\min}, E_{BS}^{i,\min}\right] \\ \leq \left[P_{BC}^{i,\max}, P_{BD}^{i,\max}, E_{BS}^{i,\max}\right] \end{cases} \tag{45}$$

$$P_{BC}^{t,i} \cdot P_{BD}^{t,i} = 0 \tag{46}$$

$$E_{BS}^{t,i} = (1 - \tau_{BS}) \cdot E_{BS}^{t-1,i} + \left(P_{BC}^{t,i} \cdot \eta_{BC} - P_{BD}^{t,i} / \eta_{BD}\right) \cdot \Delta t \tag{47}$$

$$E_{BS}^{0,i} = E_{BS}^{N_T \Delta t,i} \tag{48}$$

$$\left[H_{TC}^{t,i}, H_{TD}^{t,i}, E_{TS}^{t,i}\right] \begin{cases} \leq \left[H_{TC}^{i,\min}, H_{TD}^{i,\min}, E_{TS}^{i,\min}\right] \\ \leq \left[H_{TC}^{i,\max}, H_{TD}^{i,\max}, E_{TS}^{i,\max}\right] \end{cases} \tag{49}$$

$$H_{TC}^{t,i} \cdot H_{TD}^{t,i} = 0 \tag{50}$$

$$E_{\mathrm{TS}}^{t,i} = (1 - \tau_{TS}) \cdot E_{\mathrm{TS}}^{t-1,i} + \left(H_{\mathrm{TC}}^{t,i} \cdot \eta_{TC} - H_{\mathrm{TD}}^{t,i} / \eta_{TD}\right) \cdot \Delta t \tag{51}$$

$$E_{TS}^{0,i} = E_{TS}^{N_T \Delta t,i} \tag{52}$$

Note that in the above risk-averse MEMG coordination model, considering the thermal inertia (i.e., the thermal energy fluctuation rate is much lower than power), we mainly focus on uncertainties from active and reactive power loads ($P_{EL}^{t,i}$ and $Q_{RL}^{t,i}$) as well as active power outputs of WTs and PVs ($P_{WT}^{t,i}$ and $P_{PV}^{t,i}$) due to uncertain weather conditions and forecast inaccuracy [12]. As uncertainty sources would have infinite realizations or scenarios [11], for the concise model presentation, uncertainty scenario indices are not shown in (18)-(52) and will be detailed in Section IV.

The risk in this study refers to the "risk of the high-cost in the unfavorable scenarios" [35]. Without considering the risk, *i.e.*, risk-neutral, although the expected operation cost over the system uncertainties is low (too optimistic), there can be a high-level variance in costs of individual scenarios. If uncertainty realizations in the intra-day operation are close to those scenarios with high costs, the actual intra-day operation cost would be much higher than the day-ahead expected value. Therefore, the system decision-makers would be willing to take the risk into account, that is, choosing a solution with a slightly higher expected operation cost but a much lower variance for all stochastic scenarios [33]. As CVaR is a coherent risk measure whose effectiveness has been well justified in areas like financial and risk management, natural gas system expansion planning, and network optimization, it is applied in this study.

It is noteworthy that the objective function (23) together with constraints (30)-(42) forms a traditional VVC problem, while the objective function (19) with constraints (20)-(25), (27)-(33), (41)-(52) build a traditional risk-neutral unit commitment problem. As a consequence, by integrating the risk (26), our proposed model presents the system operation which coordinates the unit commitment and VVC in a risk-averse manner.

B. Model Convexification and Linearization

The risk-averse stochastic coordination model in (18)-(52) is non-linear and non-convex. Directly solving these nonlinear and non-convex constraints (3), (5), (12), (15), (22), (26), (34), (38), (39), (46) and (50) could result in an excessively high computation burden and low solution quality. Therefore, to improve the solution quality with favorable solution time, convexification and linearization approaches are adopted to convert the original problem into a MILP one.

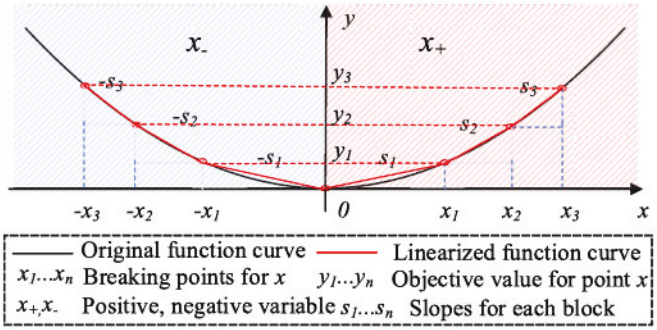

Fig. 5. Piecewise linear approximation of a convex quadratic function.

- *Linearizing thermal flow in constraints (3), (5), (12), and (15):* Although both the mass flow rate and temperature can vary to meet the thermal demands, the constant mass flow-variable temperature (CF-VT) strategy is widely used in practice [25]. In the CF-VT strategy, it assumes that the mass flow rates remain constant and only the temperature is adjusted to meet thermal demands. Under this assumption, all the nonlinear thermal flow constraints (3), (5), (12), and (15) are linear.
- *Convexifying max functions (22) and (26):* The following *Proposition 1* can be used to convexify the max functions.

Proposition 1: Each of the max functions in (22) and (26) can be equivalently represented as two linear inequalities.

Proof of Proposition 1: Take (22) for example. As the objective function (18) is monotonically increasing with C_{ST}^t, to achieve the minimum objective value, C_{ST}^t would always seek the smaller of the two terms within the max function. That is, C_{ST}^t is always their supremum. Thus, Eq. (22) can be convexified as (53). This completes the proof.

$$C_{ST}^t \geq 0; C_{ST}^t \geq \sum_{i \in N_I} \left(U_{MT}^{t,i} - U_{MT}^{t-1,i}\right) \cdot \xi_{MT}^{U,i} \tag{53}$$

- *Linearizing the polynomial function (23):* As C_{PL}^t is convex and monotonically increases with the $P_{AC}^{t,b}$ and $Q_{Re}^{t,b}$ in (23), the *upper linearization* method can be used to linearize these convex quadratic terms.

Taking $y = ax^2$ with a≥0 (the same form as (23)) in Fig. 5 for further illustration, it can be linearized as the summation of all the linear blocks in positive and negative segments as in (54).

$$\begin{aligned} y &= \sum_{k \in N_K} s_k \cdot \left(x_+^k - x_-^k\right) \\ s.t., x &= \sum_{k \in N_K} \left(x_+^k + x_-^k\right), \\ & x_{k-1} \leq x_+^k \leq x_k, -x_k \leq x_-^k \leq -x_{k-1} \end{aligned} \tag{54}$$

The lemma behind the *upper linearization* method is, given the convex objective function, Eq. (54) enforces that no value is assigned to later blocks until former ones are fully filled up.

- *Linearizing SOC constraints (34) and (38):* The PIA method can be used. Taking (34) for instance, the feasible region of this SOC constraint is a circle with radius $S_{PF}^{t,b}$ in Fig. 6.

The computation burden can be further reduced by excluding the infeasible region with the given power factor of distribution lines. With this, two polygons above and below the infeasible region can be used to approximate the original whole feasible one. Then the feasible regions can be described by the multiple linear inequality constraints corresponding to all the edges. For instance, (48) describes the inequality corresponding to edge A-B in Fig. 6(a).

$$Q_{RE}^{t,b}\cdot\left(P_B^{t,b}-P_A^{t,b}\right)-P_{AC}^{t,b}\cdot\left(Q_B^{t,b}-Q_A^{t,b}\right)\le P_B^{t,b}\cdot Q_A^{t,b}-Q_B^{t,b}\cdot P_A^{t,b} \quad (55)$$

- *Linearizing polynomial constraint (39):* Eq. (56) can be used to guarantee a fully secure operation plan against all the potential uncertainties, where ω_{WT}/ω_{PV} are factors reflecting the maximum deviation of the RES's active power outputs from its forecast $P_{WT}^{t,F}/P_{PV}^{t,F}$.

$$\pm\left[Q_{WT}^{t,i},Q_{PV}^{t,i}\right]\le\left[\sqrt{\left(S_{WT}^{i}\right)^2-\left(\omega_{WT}\cdot P_{WT}^{t,F}\right)^2},\ \sqrt{\left(S_{PV}^{i}\right)^2-\left(\omega_{PV}\cdot P_{PV}^{t,F}\right)^2}\right] \quad (56)$$

- *Relaxing bilinear terms: Proposition 2* is adopted to relax the bilinear terms in (44), (46) and (50).

Proposition 2: The bilinear terms can be directly relaxed without compromising solution optimality.

Proof of Proposition 2: Take (46) for instance. As the objective (18) is monotonically increasing with $P_{BC}^{t,i}$ and $P_{BD}^{t,i}$, if both were non-zero with $P_{BC}^{t,i}\ge P_{BD}^{t,i}$, there must exist another combination of $\underline{P}_{BC}^{t,i}$ and $\underline{P}_{BD}^{t,i}$ where $\underline{P}_{BC}^{t,i}-\underline{P}_{BD}^{t,i}=P_{BC}^{t,i}-P_{BD}^{t,i}$ with $\underline{P}_{BD}^{t,i}=0$, which produces the same net BS power input with a cheaper solution. Thus, all the bilinear constraints can be relaxed directly given the convexity nature. This completes the proof.

IV. Proposed Adaptively Stochastic Solution Approach

By leveraging the risk-averse coordinated model discussed in Section III, this section then presents the adaptive (two-layer) operation framework to address the interplay of the MEMG operations in both day-ahead and intra-day timeframes against diverse system uncertainties.

A. Adaptive (Two-Layer) Operation Framework

To effectively handle various uncertainties and make full use of distinct energy properties, the MEMG operation is designed in a two-layer structure as shown in Fig. 7.

The first layer is called the day-ahead operation that covers a relatively long operating timescale. Given the inputs on the day-ahead predictions of all system uncertainty sources as well as operation parameters, the optimal scheduling of assets that are in the first layer will then be obtained. Those decisions in this study include charging/discharging decisions of energy storage, tap positions of OLTCs, on/off status of CCHPs, position levels of CBs, and thermal flows.

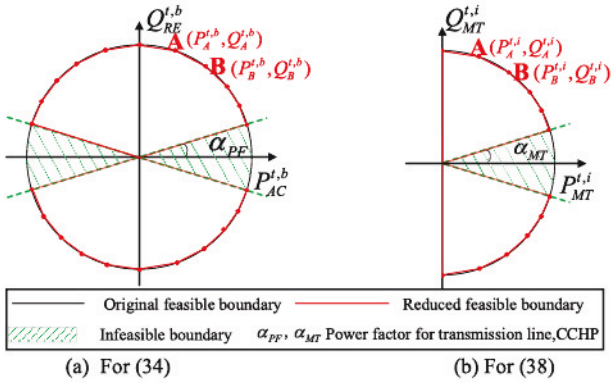

Fig. 6. Illustration of the polygonal inner approximation method.

The second layer is the intra-day operation that covers a short operating timescale, such as one hour or several minutes. The inputs are the intra-day realizations of various uncertainties and operation decisions derived in the first layer. The decisions for this layer are the active and reactive power dispatch of CCHP plants, PtC units, converter-interfaced generators, and power flow (including the power exchange with the main grid). These decisions would be updated successively and implemented to complement the first layer operation.

The two layers are classified based on the units' response speeds, functions individual units play, and distinct energy properties. Given the larger inertia (quasi-dynamics) of the thermal energy, it acts dynamically like a virtual thermal storage, and the thermal flow is scheduled in the first layer to allow thermal load shifting; BS schedule is also determined in the first layer, as they mainly play the role of the peak-shaving and flexibility enhancement over the long time horizon, and the frequent charging/ discharging could compromise its lifespan and incur high degradation cost (see Eq. (25)); Position tuning of OLTCs and CBs are also determined in the first layer, as this process is slow and cannot be achieved in real-time [14].

To this end, the compact form of the operation framework is presented in (57)-(60). Eq. (57) is the equivalent form of (18)-(26). $\mathbf{x}$ represents the first-layer variables that are related to the day-ahead operation, i.e.,E_{BS}, P_{BC}, P_{BD}, E_{TS}, H_{TC}, H_{TD}, $T_{s/r,(+)/(-)}$, N_{Tap}, N_{CB}, and U_{MT}; $\mathbf{y}$ denotes the remaining continuous decision variables in the second-layer operation, i.e., P_{MT}, H_{MT}, P_{PtC}, H_{PtC}, Q_{MT}, P_{AC}, Q_{RE}, Q_{MT}, Q_{WT}, Q_{PV}, V_{BUS}, P_{BUY}, and P_{SELL}; $\boldsymbol{d}_0$ corresponds to forecast values of all uncertainties. $\mathbf{c}^T\mathbf{x}$ includes the costs and risks associated with the first-layer decisions; $\mathbf{b}^T\mathbf{y}$-$\mathbf{e}^T\mathbf{d}_0$ refers to the operation cost associated with second-layer variables. χ is the feasible region of the day-ahead operation, described by (27), (35)-(37), and (45)-(52); Constraint (59) summarizes all the other constraints with respect to second-stage variables; Constraint (60) covers (28) and (30)-(31) to enforce the energy balance.

$$\min_{\mathbf{x},\mathbf{y}}\ \underbrace{\mathbf{c}^{\mathbf{T}}\cdot\mathbf{x}}_{\text{first layer}}+\underbrace{\mathbf{b}^{\mathbf{T}}\cdot\mathbf{y}-\mathbf{e}^{\mathbf{T}}\cdot\mathbf{d}_0}_{\text{sec ond layer}}+\rho_{\mathbf{c}}\cdot CVaR_{\alpha}\left[\underbrace{\mathbf{c}^{\mathbf{T}}\cdot\mathbf{x}}_{\text{firstlayer}}+\underbrace{\mathbf{b}^{\mathbf{T}}\cdot\mathbf{y}-\mathbf{e}^{\mathbf{T}}\cdot\mathbf{d}_0}_{\text{sec ond layer}}\right] \quad (57)$$

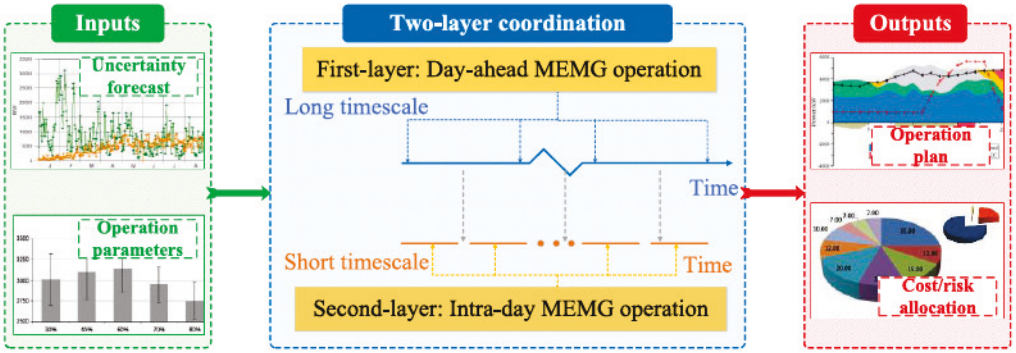

Fig. 7. The two-layer coordinated structure for the MEMG.

$$s.t., \quad \mathbf{x} \in \chi \tag{58}$$

$$\mathbf{A}\cdot\mathbf{x}+\mathbf{B}\cdot\mathbf{y}\geq\mathbf{f} \tag{59}$$

$$\mathbf{E}\cdot\mathbf{x}+\mathbf{F}\cdot\mathbf{y}=\mathbf{d}_0 \tag{60}$$

B. Adaptive SP Approach

The adaptive (two-layer) SP method is applied in this study to solve the proposed MEMG coordination model.

- *Scenario-based two-stage day-ahead optimization:* With probability distributions of all uncertainties, the Latin hypercube sampling (LHS) is applied to generate multiple uncertainty scenarios. Compared with the traditional Monte Carlo method, it spreads the sample points more evenly across all possible values by partitioning each input distribution into intervals of equal probability. Furthermore, to reduce the computational burden with numerous scenarios, the simultaneous backward reduction (SBR) approach is applied to select a limited but representative set of ones. The detailed scenario generation and reduction procedures can be referred to from [37].

Given the reduced scenario set, the day-ahead SP problem is formulated as a two-stage problem in (61)-(64), where s and N_S are index and number of scenarios; λ_s is the probability of scenario s; $\mathbf{d}_s$ is the *sth* uncertainty realization (in terms of scenarios), including the generation from WTs and PVs as well as active and reactive power loads. In (61), the expectation is calculated over all simulated second-stage scenarios. Constraints (63)-(64) denote that the second stage is optimized under $\mathbf{x}$ and constrained by $\Upsilon(\mathbf{x},\mathbf{d}_s)$. Hence, the adaptive SP method aims to find a solution that minimizes the first-stage cost and risk plus expected second-stage cost over all the simulated scenarios.

$$\min_{\mathbf{x}} \underbrace{\mathbf{c}^{\mathbf{T}}\cdot\mathbf{x}}_{\text{firststage}}+\underbrace{\sum\nolimits_{s\in N_S}\lambda_s\cdot L(\mathbf{x},\mathbf{d}_s)}_{\text{sec ondstage}} + \rho_c\cdot CVaR_\alpha\left[\underbrace{\mathbf{c}^{\mathbf{T}}\cdot\mathbf{x}}_{\text{firststage}}+\underbrace{\sum\nolimits_{s\in N_S}\lambda_s\cdot L(\mathbf{x},\mathbf{d}_s)}_{\text{sec ondstage}}\right] \tag{61}$$

$$s.t., \mathbf{x}\in\chi \tag{62}$$

where:

$$L(\mathbf{x},\mathbf{d}_s):=\min_{\mathbf{y}_s\in\Upsilon(\mathbf{x},\mathbf{d}_s)}\mathbf{b}^{\mathbf{T}}\cdot\mathbf{y}_s-\mathbf{e}^{\mathbf{T}}\cdot\mathbf{d}_s \tag{63}$$

$$\Upsilon(\mathbf{x},\mathbf{d}_s):=\left\{\mathbf{y}|\mathbf{A}\cdot\mathbf{x}+\mathbf{B}\cdot\mathbf{y}_s\geq\mathbf{f},\mathbf{E}\cdot\mathbf{x}+\mathbf{F}\cdot\mathbf{y}_s=\mathbf{d}_s\right\} \tag{64}$$

- *Intra-day optimization:* With decisions $\mathbf{x}^*$ obtained from the day-ahead optimization and the uncertainty realization $\boldsymbol{d}_0$, the intra-day operation is a single-stage deterministic model (65)-(66).

$$L(\mathbf{x}^*):=\min_{\mathbf{y}}\mathbf{b}^{\mathbf{T}}\cdot\mathbf{y}-\mathbf{e}^{\mathbf{T}}\cdot\mathbf{d}_0 \tag{65}$$

$$s.t., \ \mathbf{B}\cdot\mathbf{y}\geq\mathbf{f}-\mathbf{A}\cdot\mathbf{x}^*\cdot\mathbf{F}\cdot\mathbf{y}=\mathbf{d}_0-\mathbf{E}\cdot\mathbf{x}^* \tag{66}$$

V. Case Study

A. Testing System

A grid-tied MEMG as shown in Fig. 8 is used to verify the effectiveness of the proposed method, which includes an IEEE 33-bus radial distribution system and three 8-node thermal networks.

A winter case with the information from a typical winter day is tested. The substation voltage is set as 1.0 p.u., and the voltage limit is set as 1±0.05 p.u. The substation transformer has a 5% tap range with 20 tap positions [14]; Six CBs are installed on buses 2, 3, 6, 11, 21, and 23, with the capacity of 300 kVar each; The RESs and BS are installed on buses 4, 6,11, 13, 19, 23, and 31. CCHP plants, PtC units, and TSs are installed on buses 4, 11, and 28, and are respectively connected to thermal source nodes 1, 9, and 17. The ramp rates of CCHP plants are 30 kW/min. For the BS, its unit degradation cost per charging and discharging process is set as 0.03/kWh [31], [33]. Other system parameters can be referred to from [12].

The parameters for thermal networks are listed in Tab. I. The temperature limits of all the supply and return pipelines are set as [80,100] $°C$ and [50, 70] $°C$, respectively.

The dispatch horizon of the day-ahead operation is 24 hours with 1-hour granularity, and the intra-day operations are made every hour with the actual uncertainty realizations. Stochastic variations of RESs and power loads are set as 25% and 10% of their forecasts [6], [13], as shown in Fig. 9. Forecasts on active power generations of RESs and multi-energy demands can be derived via prediction techniques [36] using historical data. All these techniques show that the shorter the forecast

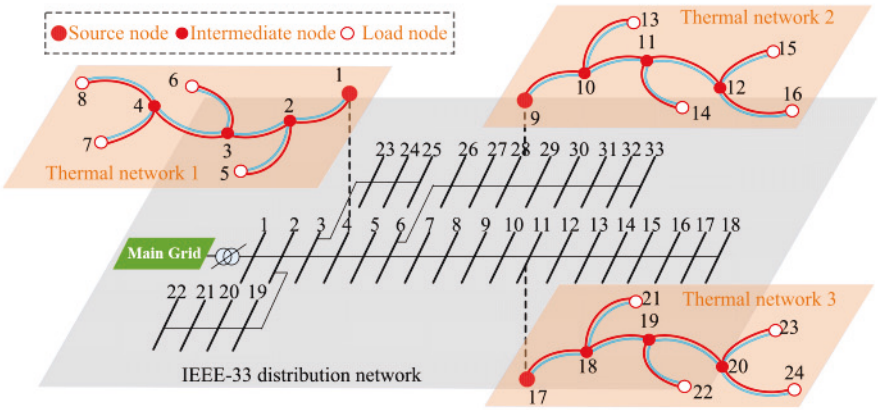

Fig. 8. Schematic diagram of the MEMG test system.

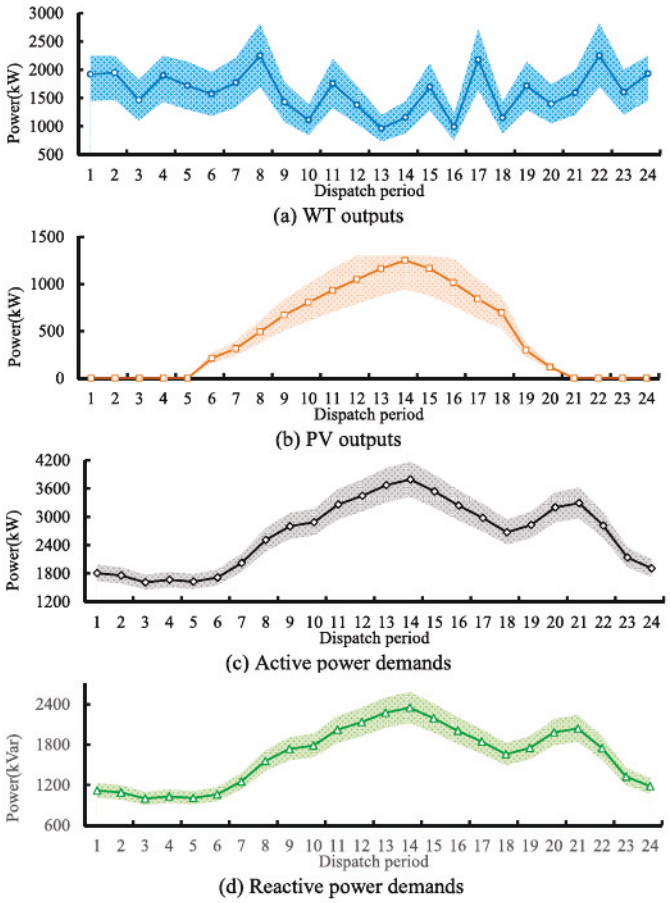

Fig. 9. Forecasts and variations of RES generation and power demands.

lead time, the more accurate the results. In terms of risk management, the confidential level is set as 0.9 and ρ_c is 0.1.

All the case studies are conducted on an Intel Xeon E5-1630 3.70GHz PC with 16G RAM and solved by Cplex on the General Algebraic Modeling System (GAMS) version 25.1.1 [38]. The relative MILP gap (67) is set as 0.01% for the sake of convergence speed and solution accuracy.

$$\text{Relativegap} = \frac{|\text{best known solution} - \text{best bound solution}|}{|\text{best bound solution}|} \quad (67)$$

TABLE I
PARAMETERS OF THE THERMAL NETWORK [19]

Pipeline (start node, end node)	Length(m)	Type	Mass flow rate/(kg/h)
(1, 2); (9, 10); (17, 18)	1050.00	DN80	23017.08
(2, 3); (10, 11); (18, 19)	525.00	DN78	20905.19
(3, 4); (11, 12); (19, 20)	525.00	DN60	12457.36
(2, 5); (10, 13); (18, 21)	525.00	DN32	2111.89
(3, 6); (11, 14); (19, 22)	225.00	DN50	8447.83
(4, 7); (12, 15); (20, 23)	525.00	DN54	10345.87
(4, 8); (12, 16); (20, 24)	225.00	DN32	2111.49

*DN is a technical term in thermal engineering that means "nominal diameter".

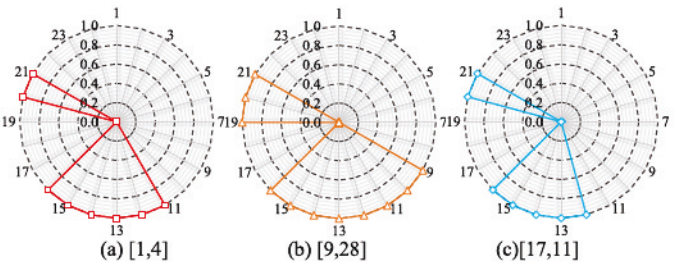

Fig. 10. Unit commitment of CCHPs: the first number denotes the node index in the thermal network, the second one is the node index in the power network.

B. Day-Ahead Operation Results

Based on the day-ahead predictions in Fig. 9, 2,000 scenarios are initially generated by the LHS method, and then reduced to 10 representative ones via the SBR method to conduct the scenario-based day-ahead optimization.

The simulation results on the unit commitment of CCHP plants, the thermal balance condition of all three thermal networks, and the temperature of thermal flows are demonstrated in Figs. 10–12, respectively.

From Figs. 10–12, it can be concluded that:

(i) The power and thermal energy dispatch are coordinated tightly. When electricity transaction prices are low, the thermal energy is mostly converted from electricity by PtC units, *i.e.*, periods 1-9 and 22-24 in Fig. 10. When electricity transaction prices are high, thermal energy is dominantly generated from CCHP plants, *i.e.*, periods 12-16 and 20-21 in Figs. 10–11;

(ii) The TS stores thermal energy when the thermal generation cost is low and then releases it when it becomes high.

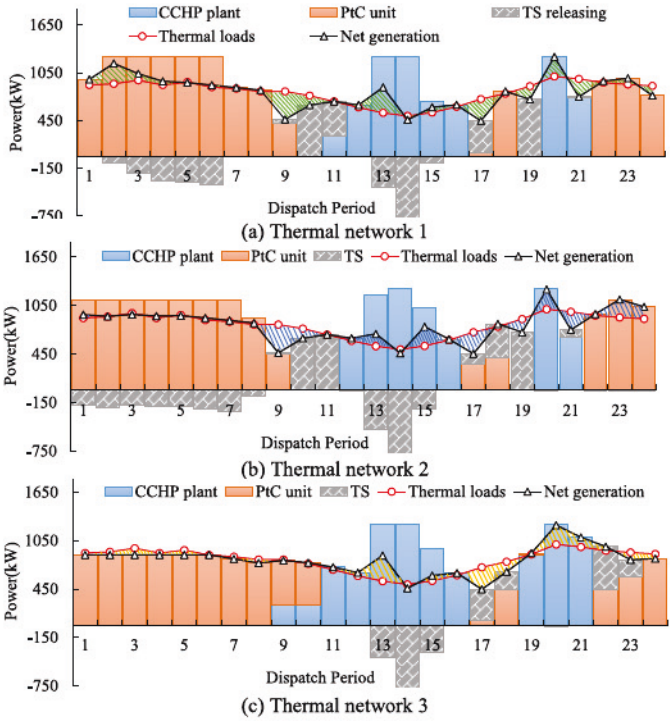

Fig. 11. The thermal energy balance condition for the three thermal networks.

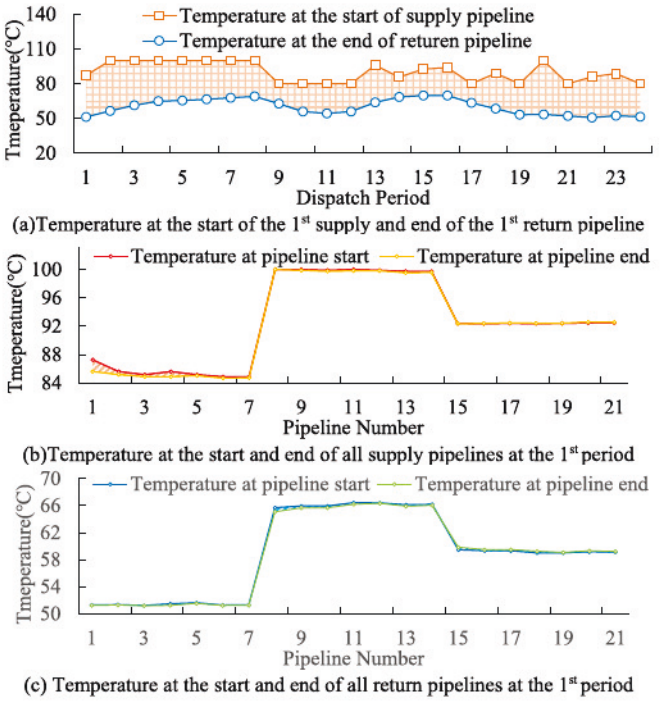

Fig. 12. The pipeline temperature for thermal flow.

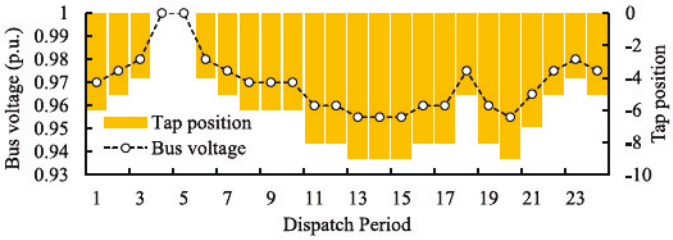

Fig. 13. Tap positions for OLTCs and voltage profile of the reference bus.

Thus, the TS can effectively reduce thermal supply cost by coordinating with CCHP plants and PtC units;

(iii) In all the thermal networks, the net thermal generation is not always equal to the thermal loads. The reason is, different from the instant power transmission, considering the thermal transmission delay makes the thermal network basically a virtual TS. The shaded area between the net generation and thermal loads in Fig. 11 indicates its storage capability;

(iv) Thermal balance condition and CCHP operation in the three thermal networks are different, though their network configura-tions are the same. This is because the thermal and power flows are tightly interdependent and thus affect one another.

(v) For thermal temperature, as indicated in (15), the shaded area in Fig. 12(a) which is the temperature difference between the start of the 1^{st} supply pipeline and the end of the 1^{st} return pipeline, represents the total thermal generation of the first thermal network. Figs. 12(b)–(c) show that for the same supply pipeline [Fig. 12(b)] and return [Fig. 12(c)] pipeline, the start, and end temperature are different, indicating the storage capability (the shaded area) of thermal networks as shown in Fig. 11.

Tap positions of OLTCs and voltage profiles of the reference bus are shown in Fig. 13. It can be seen that the tap positions are negative most of the time, reflecting that the primary bus voltage is lower than the nominal level. The reason is, a large amount of RESs could cause system overvoltage, hence, to avoid the potential overvoltage issue, the voltage of the reference bus is set slightly lower than 1 p.u.

The day-ahead operation results indicate the effectiveness of our proposed method. The corresponding operation cost and CVaR for the MEMG are 2855.39$ and 2844.50$. The solution time is 94.09s. The computational performance shows that our MILP model is fully compatible with the day-ahead operation.

C. Intra-Day Operation Results

For the intra-day MEMG operation, with hourly realizations of various uncertainties, the active and reactive power balance conditions are depicted in Fig. 14.

Form Fig. 14(a), it can be inferred that:

(i) The same as the thermal energy balance performance in Fig. 10, CCHP plants and PtC units can leverage the differences of electricity prices and multi-energy loads among all dispatch periods to pursue their optimal energy generation decisions.

(ii) The BSs could collaborate with other assets to shift power loads for peak-shaving and cost-saving purposes. That is, BSs charge at periods 4-6 when electricity transaction prices are low while discharging at high transaction prices periods 13-15. Besides, BSs are not charged or discharged frequently over the entire dispatch horizon, this is because given (25), the frequent charging and discharging of the BSs would lead to high battery degradation cost.

(iii) The MEMG sells electricity at high electricity transaction prices periods 12-16 and 20-21 but purchases electricity

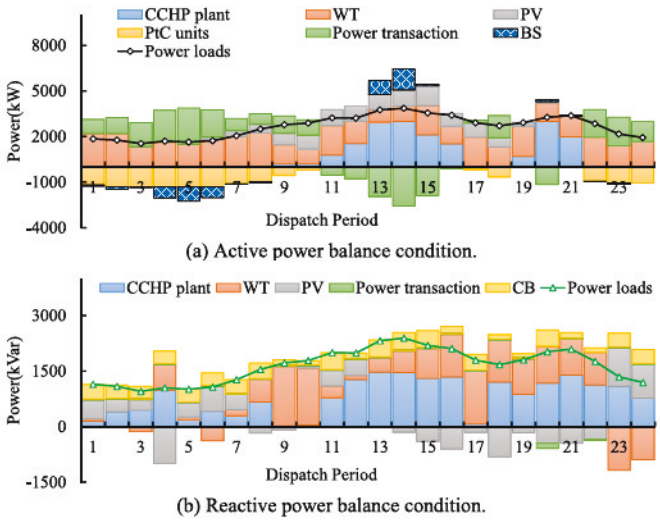

(a) Active power balance condition.

(b) Reactive power balance condition.

Fig. 14. Intra-day power dispatch results for the MEMG.

to satisfy its internal multi-energy loads at low electricity transaction price periods 1-10,18-19, and 22-24.

For the reactive power balance condition in Fig. 14(b), it shows that all the electronic converters of generators (WTs, PVs, CCHP plants) and CBs cover most of the reactive power loads locally, while the main grid provides very limited support. This is because the main grid contributes to reactive power balance through the OLTCs as in Fig. 13. From (19), if a large amount of reactive power flows from the main grid to the individual buses, higher power losses will be incurred. Thus, the MEMG prefers to satisfy its active power demands locally.

The intra-day operation results demonstrate that our proposed method is effective for coordinating all the generators, reactive power devices, and energy storage assets for both optimal active and reactive power management. With the intra-day MEMG operation, the final 24-hour operation cost for the MEMG is 2981.54$ with a solution time of 1.83s only. This solution performance also indicates that our method is applicable to the intra-day operation.

D. Comparison With Other Approaches

To further demonstrate the effectiveness of our proposed method, three MEMG operation benchmarks are compared:

- ***M1:*** No thermal network model is involved in this method [11], [12]. That is, this method assumes that there is no practical thermal network and thermal sources, and loads are single-bus connected;
- ***M2:*** No centralized VVC scheme is considered in this method [5]–[6], [11]–[12]. That is, there is no coordination between the active and reactive power dispatch, all the reactive power are satisfied only by the utility grid;
- ***M3:*** This is the risk-natural SP method [7]–[11]. This method does not consider risks in the MEMG operation, i.e., $\rho_c = 0$;

Results of the three benchmarks are presented in Table II. For a clear comparison, the results of our method are also listed. All the simulation results demonstrate that:

(i) For ***M1***, the cost and risk of the day-ahead layer, as well as the cost of the intra-day layer are all higher than our method. This is because ***M1*** neglects thermal flows and cannot fully utilize the large thermal inertia rising from the thermal network, which otherwise could provide additional system dispatch flexibility. The comparison verifies the potential benefits of considering the thermal network in practical applications.

TABLE II
SIMULATION RESULTS OF ALL METHODS IN WINTER

Item		M1	M2	M3	Our Method
First layer	Cost	2907.11$	2971.73$	2851.74$	**2855.39$**
	CVaR	2895.7$	2965.18$	-	**2844.50$**
	Solution time	59.89s	60.13s	60.83s	**94.09s**
Second layer	Cost	3033.54$	3099.90$	2989.24$	**2981.54$**
	Solution time	1.84s	1.79s	1.82s	**1.83s**

(ii) When the VVC scheme is not considered in ***M2***, all the system reactive power needs are satisfied by the main grid. However, transmitting a large amount of active power from the main grid (the first bus) to all other buses will incur high power losses. Thus, the cost and risk of ***M2*** are higher than our method in both day-ahead and intraday layers. This shows the necessity of coordinating active and reactive power.

(iii) When the risk is neglected in ***M3*** (i.e., risk-neutral), the day-ahead operation cost is lower than our proposed method. However, its intra-day operation cost is higher. The reason is that neglecting the risk in the day-ahead operation could induce overly optimistic decisions, that is, there can be a low day-ahead operation cost but high variance among all stochastic scenarios. Thus, when uncertainty realizations in the intra-day operation are close to those scenarios with high costs, ***M3*** would lead to high intra-day operation costs. The cost comparison indicates the effectiveness of considering risks in the system coordination.

E. Sensitivity Analysis for Different Typical Days

To further demonstrate the effectiveness of our system-wide coordination model for the MEMGs under different application occasions, case studies for typical days of summer and transition seasons (spring and fall) are conducted.

For both the summer and transition seasons, locations of all the distributed units and system parameters (including operation limits for generators, networks, power transaction prices between MEMGs and main grid, substation voltage, unit adjustment level for CBs, substation tap range, heterogeneous energy storage) remain the same as the winter case. However, for the summer case, space cooling demands are needed with TS referring to the cooling one specifically; For transition seasons, the hot water demands are required instead [39].

The forecasts of the RES outputs and multi-energy demands for both the summer and transition seasons are given in Fig. 15. Still, without loss of generality, any other real-world data inputs can be applied without affecting the effectiveness of the proposed method.

After the simulation, the day-ahead and intra-day operation results from all the methods, including the operation cost, risk, and computation time, are given in Tables III and IV. From Tables III and IV, it can be seen that the same with the winter case in Table II, our proposed method is effective and efficient for reducing the MEMG operation cost and immunizing against diverse system uncertainties with a satisfactory

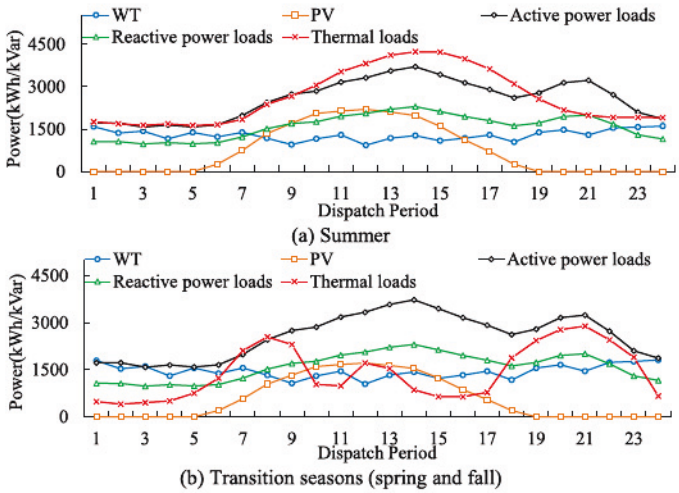

Fig. 15. The forecasts of the RES outputs and multi-energy demands for both the summer and transition seasons.

TABLE III
SIMULATION RESULTS OF ALL METHODS IN SUMMER

Item		M1	M2	M3	Our Method
First Layer	Cost	2541.86$	2613.20$	2501.93$	**2511.18$**
	CVaR	2521.15$	2597.30$	-	**2495.96$**
	Solution time	74.97s	81.354s	72.30s	**120.54s**
Second Layer	Cost	2634.27$	2708.12$	2615.25$	**2604.01$**
	Solution time	1.85s	1.81s	1.82s	**1.86s**

TABLE IV
SIMULATION RESULTS OF ALL METHODS IN TRANSITION SEASONS

Item		M1	M2	M3	Our Method
First Layer	Cost	2150.67$	2247.22$	2118.19$	**2129.95$**
	CVaR	2179.07$	2280.14$	-	**2156.60$**
	Solution time	70.89s	80.99s	60.83s	**101.36s**
Second Layer	Cost	2264.07$	2362.84$	2256.084$	**2241.81$**
	Solution time	1.81s	1.82s	1.81s	**1.80s**

computational performance for coordinating the active power, reactive power, and practical thermal flow in a risk-averse manner.

To this end, all simulation results indicate the effectiveness of our proposed method. For the real-world applications, on the one hand, unit commitment status and system coordination decision results obtained from our proposed method could be sent to the MEMG energy management system as references for their actual physical operation. On the other hand, the operation decisions can be used as setpoints for the optimal system control, which can be implemented in the hardware platform [40]. It is also noteworthy that there can be other emerging algorithms like machine learning and artificial intelligence-based algorithms, to solve the raw nonlinear problems with potentially good performance, which will be explored in our future work.

VI. CONCLUSION

In this paper, an adaptive risk-averse SP approach for MEMGs is presented while considering the various system uncertainties, VVC scheme, realistic thermal flow, and battery degradation. The proposed approach can effectively coordinate the active, reactive power, and thermal energy to reduce the overall operation cost and risk. Numerical case studies are conducted to illustrate that:

(i) The proposed method can effectively and efficiently coordinate active power, reactive power, and thermal energy in the day-ahead and intra-day operations.

(ii) Considering realistic thermal flow model could leverage the distinct roles of different energy, especially the thermal inertia, in saving costs and reducing risks;

(iii) Involving the VVC scheme can be highly effective to coordinate the active and reactive power dispatch;

(iv) The risk management is important for decision-makers to immunize the system operation against diverse uncertainties;

For future work, the reinforcement learning-based real-time system control with hardware implementation for the MEMGs can be conducted to evaluate how the system reacts to real-time control signals [40]. In addition, advanced algorithms can be developed to solve the original nonlinear/nonconvex models efficiently while the state-of-art forecasting techniques which contribute to obtaining more accurate predictions on uncertainty sources can be applied for the MEMG operation. Finally, the optimal energy management, energy trading, and profit allocation problems among multiple MEMGs are also potential future research directions [41].

REFERENCES

[1] E. Guelpa, A. Bischi, V. Verda, M. Chertkov, and H. Lund, "Towards future infrastructures for sustainable multi-energy systems: A review," *Energy*, vol. 184, pp. 2–21, Oct. 2019.

[2] W. B. Powell and S. Meisel, "Tutorial on stochastic optimization in energy—Part I: Modeling and policies," *IEEE Trans. Power Syst.*, vol. 31, no. 2, pp. 1459–1467, Mar. 2016.

[3] A. A. Lekvan, R. Habibifar, M. Moradi, M. Khoshjahan, S. Nojavan, and K. Jermsittiparsert, "Robust optimization of renewable-based multi-energy micro-grid integrated with flexible energy conversion and storage devices," *Sustain. Cities. Soc.*, vol. 64, Jan. 2021.

[4] X. Lu, Z. Liu, L. Ma, L. Wang, K. Zhou, and N. Feng, "A robust optimization approach for optimal load dispatch of community energy hub," *Appl. Energ.*, vol. 259, Feb. 2020.

[5] X. Lu, Z. Liu, L. Ma, L. Wang, K. Zhou, and S. Yang, "A robust optimization approach for coordinated operation of multiple energy hubs," *Energy*, vol. 197, Apr. 2020.

[6] C. Zhang, Z. Y. Dong, and Y. Xu, "Two-stage robust operation for islanded multi-energy micro-grids," in *Proc. 11th IET Int. Conf. Adv. Power Syst. Control Oper. Manage. (APSCOM)*, Hong Kong, 2018, pp. 1–6.

[7] C. Zhang, Y. Xu, and Z. Y. Dong, "Robustly coordinated operation of a multi-energy micro-grid in grid-connected and islanded modes under uncertainties," *IEEE Trans. Sustain. Energ.*, vol. 11, no. 2, pp. 640–651, Apr. 2020.

[8] M. Aghamohamadi and A. Mahmoudi, "From bidding strategy in smart grid toward integrated bidding strategy in smart multi-energy systems, an adaptive robust solution approach," *Energy*, vol. 183, pp. 75–91, Sep. 2019.

[9] A. Dolatabadi, M. Jadidbonab, B. Mohammadi-Ivatloo, "Short-term scheduling strategy for wind-based energy hub: A hybrid stochastic/IGDT approach," *IEEE Trans. Sustain. Energ.*, vol. 10, no. 1, pp. 438–448, Jan. 2019.

[10] M. Sedighizadeh, M. Esmaili, and N. Mohammadkhani, "Stochastic multi-objective energy management in residential microgrids with combined cooling, heating, and power units considering battery energy storage systems and plug-in hybrid electric vehicles," *J. Clean. Prod.*, vol. 195, pp. 301–317, Sep. 2018.

[11] J. Wang, C. Zhang, S. You, Y. Zong, C. Træholt, Z. Y. Dong, "Multi-timescale coordinated operation of a CHP plant-wind farm portfolio considering multiple uncertainties," *Int. J. Elect. Power Energy Syst.*, vol. 125, Feb. 2021.

[12] Z. Li and Y. Xu, "Temporally-coordinated optimal operation of a multi-energy microgrid under diverse uncertainties," *Appl. Energy*, vol. 240, pp. 719–729, Apr. 2019.
[13] B. Wei, X. Han, P. Wang, H. Yu, W. Li, and L. Guo, "Temporally coordinated energy management for AC/DC hybrid microgrid considering dynamic conversion efficiency of bidirectional AC/DC converter," *IEEE Access*, vol. 8, pp. 70878–70889, 2020.
[14] Y. Xu, Z. Y. Dong, R. Zhang, and D. J. Hill, "Multi-timescale coordinated voltage/var control of high renewable-penetrated distribution systems," *IEEE Trans. Power. Syst.*, vol. 32, no. 6, pp. 4398–4408, Nov. 2017.
[15] F. Qiao and J. Ma, "Voltage/Var control for hybrid distribution networks using decomposition-based multiobjective evolutionary algorithm," *IEEE Access*, vol. 8, pp. 12015–12025, 2020.
[16] Y. Guo, H. Gao, H. Xing, Q. Wu, and Z. Lin, "Decentralized coordinated voltage control for VSC-HVDC connected wind farms based on ADMM," *IEEE Trans. Sustain. Energy*, vol. 10, no. 2, pp. 800–810, Apr. 2019.
[17] K. Mahmoud, M. M. Hussein, M. Abdel-Nasser, and M. Lehtonen, "Optimal voltage control in distribution systems with intermittent PV using multiobjective Grey-Wolf-lévy optimizer," *IEEE Syst. J.*, vol. 14, no. 1, pp. 760–770, Mar. 2020.
[18] R. Zafar, J. Ravishankar, J. E. Fletcher, and H. R. Pota, "Multi-timescale model predictive control of battery energy storage system using conic relaxation in smart distribution grids," *IEEE Trans. Power Syst.*, vol. 33, no. 6, pp. 7152–7161, Nov. 2018.
[19] D. Jin, H.-D. Chiang, and P. Li, "Two-timescale multi-objective coordinated Volt/Var optimization for active distribution networks," *IEEE Trans. Power Syst.*, vol. 34, no. 6, pp. 4418–4428, Nov. 2019.
[20] Z. Liang, Q. Alsafasfeh, T. Jin, H. Pourbabak, and W. Su, "Risk-constrained optimal energy management for virtual power plants considering correlated demand response," *IEEE Trans. Smart Grid*, vol. 10, no. 2, pp. 1577–1587, Mar. 2019.
[21] W. Gu, J. Wang, S. Lu, Z. Luo, and C. Wu, "Optimal operation for integrated energy system considering thermal inertia of district heating network and buildings," *Appl. Energy*, vol. 199, pp. 234–246, Aug. 2017.
[22] X. Xu, Z. Yan, M. Shahidehpour, Z. Li, M. Yan, and X. Kong, "Data-driven risk-averse two-stage optimal stochastic scheduling of energy and reserve with correlated wind power," *IEEE Trans Sustain. Energy*, vol. 11, no. 1, pp. 436–447, Jan. 2020.
[23] B. Vatandoust, A. Ahmadian, M. A. Golkar, A. Elkamel, A. Almansoori, and M. Ghaljehei, "Risk-averse optimal bidding of electric vehicles and energy storage aggregator in day-ahead frequency regulation market," *IEEE Trans. Power Syst.*, vol. 34, no. 3, pp. 2036–2047, May 2019.
[24] W.-J. Ma, C. Oh, Y. Liu, D. Dentcheva, and M. M. Zavlanos, "Risk-averse access point selection in wireless communication networks," *IEEE Trans. Control Netw. Syst.*, vol. 6, no. 1, pp. 24–36, Mar. 2019.
[25] T. Ma, J. Wu, and L. Hao, "Energy flow modeling and optimal operation analysis of the micro energy grid based on energy hub," *Energy Convers. Manag.*, vol. 133, pp. 292–306, Feb. 2017.
[26] Z. Li, W. Wu, M. Shahidehpour, J. Wang, and B. Zhang, "Combined heat and power dispatch considering pipeline energy storage of district heating network," *IEEE Trans. Sustain. Energy*, vol. 7, no. 1, pp. 12–22, Jan. 2016.
[27] A. Barré, B. Deguilhem, S. Grolleau, M. Gérard, F. Suard, and D. Riu, "A review on lithium-ion battery aging mechanisms and estimations for automotive applications," *J. Power Sources*, vol. 241, pp. 680–689, Nov. 2013.
[28] C. Ju, P. Wang, L. Goel, and Y. Xu, "A two-layer energy management system for microgrids with hybrid energy storage considering degradation costs," *IEEE Trans. Smart Grid*, vol. 9, no. 6, pp. 6047–6057, Nov. 2018.
[29] S. Sharma, Y. Xu, A. Verma, and B. K. Panigrahi, "Time-coordinated multienergy management of smart buildings under uncertainties," *IEEE Trans Ind. Informat.*, vol. 15, no. 8, pp. 4788–4798, Aug. 2019.
[30] B. Zhou, X. Liu, Y. Cao, C. Li, C. Y. Chung, and K. W. Chan, "Optimal scheduling of virtual power plant with battery degradation cost," *IET Gener. Transm. Distrib.*, vol. 10, no. 3, pp. 712–725, 2016.
[31] A. Ahmadi, A. E. Nezhad, and B. Hredzak, "Security-constrained unit commitment in presence of lithium-ion battery storage units using information-gap decision theory," *IEEE Trans. Ind. Informat.*, vol. 15, no. 1, pp. 148–157, Jan. 2019.
[32] L. An, J. Duan, M.-Y. Chow, and A. Duel-Hallen, "A distributed and resilient bargaining game for weather-predictive microgrid energy cooperation," *IEEE Trans. Ind. Informat.*, vol. 15, no. 8, pp. 4721–4730, Aug. 2019.
[33] Z. Yuan and M.-Y. Chow, "Microgrid cooperative distributed energy scheduling (CoDES) considering battery degradation cost," in *Proc. IEEE 25th Int. Symp. Ind. Electron.*, Santa Clara, CA, USA, 2016, pp. 720–725.
[34] Z. Wang, B. Chen, J. Wang, and J. Kim, "Decentralized energy management system for networked microgrids in grid-connected and islanded modes," *IEEE Trans. Smart Grid*, vol. 7, no. 2, pp. 1097–1105, Mar. 2016.
[35] M. Roustai, M. Rayati, A. Sheikhi, and A. Ranjbar, "A scenario-based optimization of smart energy hub operation in a stochastic environment using conditional-value-at-risk," *Sustain. Cities. Soc.*, vol. 39, pp. 309–316, May 2018.
[36] W. Kong, Z. Y. Dong, Y. Jia, D. J. Hill, Y. Xu, and Y. Zhang, "Short-term residential load forecasting based on LSTM recurrent neural network," *IEEE Trans. Smart Grid*, vol. 10, no. 1, pp. 841–851, Jan. 2019.
[37] Y. Chen, X. Feng, Z. Li, Y. Xu, and A. Miragha, "Multi-stage coordinated operation of a multi-energy microgrid with residential demand response under diverse uncertainties," *Energy Convers. Econ.*, vol. 1, no. 1, pp. 20–33, 2020.
[38] (Feb. 2021). *The General Algebraic Modeling System (GAMS)-The One-Stop Solution for Your Mathematical Programming Needs*. [Online]. Available: https://www.gams.com/
[39] Z. Li, Y. Xu, X. Feng, and Q. Wu, "Optimal stochastic deployment of heterogeneous energy storage in a residential multienergy microgrid with demand-side management," *IEEE Trans. Ind. Informat.*, vol. 17, no. 2, pp. 991–1003, Feb. 2021.
[40] J. Duan, Z. Yi, D. Shi, C. Lin, X. Lu, and Z. Wang, "Reinforcement-learning-based optimal control of hybrid energy storage systems in hybrid AC–DC microgrids," *IEEE Trans. Ind. Informat.*, vol. 15, no. 9, pp. 5355–5364, Sep. 2019.
[41] Y. Li *et al.*, "Optimal operation of multimicrogrids via cooperative energy and reserve scheduling," *IEEE Trans. Ind. Informat.*, vol. 14, no. 8, pp. 3459–3468, Aug. 2018.

Zhengmao Li (Member, IEEE) received the B.E. degree in information engineering and the M.E. degree in electrical engineering from Shandong University, Ji'nan, China, in 2013 and 2016, respectively, and the Ph.D. degree in electrical engineering from the School of Electrical and Electronic Engineering, Nanyang Technological University, Singapore, in 2020.

He is a Research Fellow with the Stevens Institute of Technology, Hoboken, NJ, USA, from 2020 to 2021. His research interests include renewable energy integration, multienergy systems, such as multi-energy microgrids, multi-energy ships, optimization, and reinforcement learning techniques, such as approximate dynamic programming, robust and stochastic optimization method, the resilience of multienergy systems.

Lei Wu (Senior Member, IEEE) received the B.S. degree in electrical engineering and the M.S. degree in systems engineering from Xi'an Jiaotong University, Xi'an, China, in 2001 and 2004, respectively, and the Ph.D. degree in electrical engineering from the Illinois Institute of Technology (IIT), Chicago, IL, USA, in 2008.

From 2008 to 2010, he was a Senior Research Associate with the Robert W. Galvin Center for Electricity Innovation, IIT. He was a summer Visiting Faculty with NYISO in 2012. He was a Professor with the Electrical and Computer Engineering Department, Clarkson University, Potsdam, NY, USA, till 2018. He is currently a Professor with the Electrical and Computer Engineering Department, Stevens Institute of Technology, Hoboken, NJ, USA. His research interests include power systems operation and planning, energy economics, and community resilience microgrid.

Yan Xu (Senior Member, IEEE) received the B.E. and M.E degrees from the South China University of Technology, Guangzhou, China, in 2008 and 2011, respectively, and the Ph.D. degree from the University of Newcastle, Australia, in 2013.

He conducted postdoctoral research with the University of Sydney Postdoctoral Fellowship, and then joined Nanyang Technological University (NTU) with the Nanyang Assistant Professorship. He is currently an Associate Professor with the School of Electrical and Electronic Engineering and the Cluster Director with Energy Research Institute, NTU. His research interests include power system stability and control, microgrid, and data-analytics for smart grid applications. He is an Editor for IEEE TRANSACTIONS ON SMART GRID, IEEE TRANSACTIONS ON POWER SYSTEMS, *IET Generation, Transmission and Distribution Journals*, *IET Energy Conversion and Economics*, and China's power engineering international journals, *CSEE Journal of Power and Energy Systems* and *Journal of Modern Power System and Clean Energy*. He is also serving as the Chairman for IEEE Power and Energy Society Singapore Chapter.